

High-resolution characterization of the martensite-austenite constituent in a carbide-free bainitic steel

Hofer, Christina; Bliznuk, Vitaliy; Verdiere, An; Petrov, Roumen; Winkelhofer, Florian; Clemens, Helmut; Primig, Sophie

DOI

[10.1016/j.matchar.2018.07.011](https://doi.org/10.1016/j.matchar.2018.07.011)

Publication date

2018

Document Version

Accepted author manuscript

Published in

Materials Characterization

Citation (APA)

Hofer, C., Bliznuk, V., Verdiere, A., Petrov, R., Winkelhofer, F., Clemens, H., & Primig, S. (2018). High-resolution characterization of the martensite-austenite constituent in a carbide-free bainitic steel. *Materials Characterization*, 144, 182-190. <https://doi.org/10.1016/j.matchar.2018.07.011>

Important note

To cite this publication, please use the final published version (if applicable). Please check the document version above.

Copyright

Other than for strictly personal use, it is not permitted to download, forward or distribute the text or part of it, without the consent of the author(s) and/or copyright holder(s), unless the work is under an open content license such as Creative Commons.

Takedown policy

Please contact us and provide details if you believe this document breaches copyrights. We will remove access to the work immediately and investigate your claim.

High-resolution characterization of the martensite-austenite constituent in a carbide-free bainitic steel

Christina Hofer^{a*}, Vitaliy Bliznuk^b, An Verdiere^b, Roumen Petrov^{b,c}, Florian Winkelhofer^d, Helmut Clemens^a, Sophie Primig^{a,e}

^a*Department of Physical Metallurgy and Materials Testing, Montanuniversität Leoben, Franz-Josef-Straße 18, 8700 Leoben, Austria*

^b*Department of Electrical Energy, Metals, Mechanical Constructions and Systems, Ghent University, Tech Lane Ghent Science Park – Campus A, Technologiepark 903, 9052 Zwijnaarde, Ghent, Belgium*

^c*Department Materials Science and Engineering, TU Delft, Mekelweg 2, 2628 CD Delft, The Netherlands*

^d*Research and Development – Business Unit Coil, voestalpine Stahl GmbH, voestalpine-Strasse 3, 4020 Linz, Austria*

^e*School of Materials Science & Engineering, UNSW Sydney, 2052 NSW, Australia*

**Corresponding author. Tel: +43 3842 402 4250; fax: +43 3842 402 4202.*

E-mail address: christina.hofer@unileoben.ac.at

Abstract

The multiphase microstructure of carbide-free bainitic steels comprises bainitic ferrite laths, retained austenite with different morphologies, a minor fraction of carbides and so-called martensite-austenite areas, which partially transform during the last cooling step. While the other constituent received much attention, little is known about the structure of the martensite-austenite constituents in carbide-free bainitic steels. Thus, in this study, they were structurally and chemically investigated by high-resolution techniques such as transmission electron microscopy and atom probe tomography after preceded unambiguous identification by electron backscatter diffraction in conventional as well as transmission mode. The results, ranging from carbon segregation to cementite precipitation in the martensitic part, indicate strong auto-tempering during final cooling which is followed by aging. Also, some kind of structural modulation in the austenite belonging to the martensite-austenite areas was observed. Atom probe tomography revealed a heterogeneous carbon distribution, further supporting the findings by transmission electron microscopy.

Highlights:

- Microstructural characterization of martensite-austenite (M-A) areas by TKD and TEM
- Auto-tempering effects ranging from C clustering to carbide formation in martensite
- Signs of structural modulation of austenite in M-A areas by electron diffraction
- Heterogeneous C distribution within M-A areas due to auto-tempering during cooling

Keywords:

Carbide-free bainite; martensite-austenite constituent; transmission electron microscopy; atom probe tomography; structural modulation;

1. Introduction

Increasing demands on safety and energy efficiency in the automotive industry require new high-strength steels that still can be produced economically. In recent years, quenching-and-partitioning (Q&P) as well as carbide-free bainitic steels have shown to meet these requirements owing to their complex microstructure and resulting mechanical properties, e.g. see [1–4]. The combination of a hard matrix and a soft second phase accomplishes high strength with good elongation at the same time. Unlike dual-phase steels, where the hard and soft phase are both present in polygonal form, Q&P and carbide-free bainitic steels exhibit very homogeneous and fine acicular microstructures. This additionally enhances the impact toughness, impedes crack initiation and improves formability [5].

Beside their economic alloying concept, carbide-free bainitic steels also have a straightforward heat treatment. They are produced via austenitization followed by an isothermal heat treatment in the bainitic temperature range between 300-450°C. During the isothermal holding time, austenite transforms into carbon-supersaturated bainite. Since bainitic ferrite can only accommodate very low amounts of carbon interstitially, the excess carbon diffuses out of the bainitic ferrite sub-units directly after their formation. Due to the high silicon content (1.5-2 mass%), which has very low solubility in cementite, the driving force for cementite precipitation is drastically reduced, leading to an effective suppression of its formation during short holding times and moderate carbon supersaturation [6]. Therefore, the carbon is available to enrich the remaining austenite [1,2,6–10]. The nm-sized austenite films between individual bainitic ferrite sub-units become highly enriched in carbon, whereas carbon partitioning into blocky austenite areas in between single sheaves of bainite progresses to a far lesser extent. Thus, in these areas lower carbon contents persist [11]. Upon further cooling, the highly enriched films of austenite remain stable until room temperature, but parts of the blocky austenite may transform to martensite, forming the so-called martensite-austenite (M-A) constituent.

Although the M-A constituent represents a small fraction of the microstructure, it has a significant impact on the mechanical properties of the final steel product. It has been

shown that large areas of M-A constituent dramatically decrease the impact toughness of the steel because they act as crack initiation sites [12–14]. The reasons therefore either lie in the high brittleness of the freshly formed plate-type martensite or in the stresses induced by the volume increase due to the martensitic transformation [12]. However, Lan et al. [15] found that very small areas of M-A constituent ($<1\ \mu\text{m}$) can effectively inhibit crack propagation by deflection of the crack and, therefore, increase the impact toughness. Nevertheless, it should be kept in mind that further factors such as carbides and bainite packet size influence the toughness.

As a result of the carbon redistribution during the bainitic transformation, M-A areas have an elevated carbon content compared to their nominal composition which was verified by electron probe microanalysis [16–18] and atom probe tomography (APT) [19]. The boundaries remain partly austenitic whereby the center is mainly martensitic according to electron backscatter diffraction (EBSD), where the M-A areas are identified based on their lower diffraction pattern quality which results from the higher dislocation density [18–20].

Transmission electron microscopy (TEM) investigations revealed that the martensitic center of the M-A areas consists of plate martensite made up of micro-twins [12,13,15–17]. However, the identification of the M-A constituent in the TEM is not straightforward, since phase identification solely based on the contrast in bright field mode is not possible, considering that contrast changes according to the crystal orientation upon tilting. This issue can be overcome by the identification of the M-A constituent in the scanning electron microscope (SEM) by means of an EBSD scan. Subsequently, a site-specific specimen preparation can be carried out in the focused ion beam (FIB) microscope, applying the lift-out technique [21]. However, this has the disadvantage that the bombardment and implantation of the area of interest with focused ions can lead to the transformation of meta-stable retained austenite even at low voltage and current [22,23], and therefore distorts the observed results.

Since there is still a lack of information regarding the structure and composition of the M-A constituent in low carbon steels, this study aims to provide new information by high-resolution microscopy of this complex feature in a carbide-free bainitic steel. Based on

the correlative microscopy approach suggested by the authors in previous work [24], where the M-A areas were unambiguously identified on a conventional TEM specimen by transmission Kikuchi diffraction (TKD) [25–27] in the SEM prior to TEM investigations, a detailed TEM diffraction study of the M-A areas is presented in this paper. Thereby, the M-A constituent was also identified based on their lower diffraction pattern quality (as in conventional EBSD), and subsequently the very same area was investigated by TEM. By application of this correlative approach, new insights into the structure of these complex features have been gained. Additionally, an attempt was made to prove the findings of the TEM investigations by APT, which is the only method for chemical analysis at the atomic scale.

2. Experimental

The chemical composition (in at% and mass%) of the studied carbide-free bainitic steel is given in Table 1. The material was provided as industrial grade in the form of cold-rolled sheets with a thickness of 1.2 mm. The inductive heat treatment of samples with a size of 10x5x1.2 mm³ was carried out in a dilatometer DIL805A from TA Instruments using a type S thermocouple. Full austenitization at 900°C for 60 s was followed by quenching to an isothermal holding temperature of 400°C, which is about 50°C above the martensite start (M_s) temperature [19]. The samples were held in the bainitic temperature range for 1000 s, and subsequently quenched to room temperature. Quenching was carried out with helium gas and a cooling rate of 100°C/s to prevent other phase transformations.

The microstructure was examined by light optical microscopy (LOM) after LePera etching [28] following the practical procedure described in [19].

TEM specimens of the as-heat treated material were prepared by mechanically thinning the sheets to a thickness of 100 μm . Then, disks with a diameter of 3 mm were punched out and electropolished with a TenuPol-5 twin-jet polisher from Struers. A solution of 4 vol% perchloric acid and 96 vol% acetic acid (CH_3COOH) and a voltage of 15 V with a flow rate of 10 at room temperature were found to be best suitable. Prior to the TEM

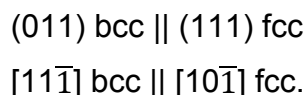
investigations the specimens were investigated via TKD in a SEM to identify the M-A constituent with the detailed set-up reported elsewhere [24]. For EBSD and TKD analyses either a field-emission gun SEM Quanta 450 or a dual-beam SEM/FIB Versa 3D from FEI equipped with a Hikari XP EBSD system from EDAX were used. TKD scans were carried out at an effective tilt angle of -10° to the incident electron beam at a working distance of 6 mm with an acceleration voltage of 30 kV, a spot size of 5, a step size of 60 nm, and 4x4 binning. Subsequently, the same regions on the sample were investigated in a JEM-2200FS TEM from JEOL equipped with a C_s corrector for the objective lens operated at a voltage of 200 kV. The schematic spot diffraction patterns were simulated with the software JEMS and the stereographic projection with the software ELDIST [29]. Cementite was described by the space group $Pbnm$ with the lattice parameters $a=4.5230 \text{ \AA}$, $b=5.0890 \text{ \AA}$ and $c=6.7428 \text{ \AA}$.

For APT investigations the M-A constituent was identified by means of conventional EBSD on a bulk sample prior to the site-specific tip preparation in the SEM/FIB. After grinding and polishing, the samples were electropolished with a Lectro-Pol V from Struers for 10 s using the A2 electrolyte, a voltage of 40 V and a flow rate of 10. The resulting surface relief was removed by gently polishing the surface with OP-U for 20 min according to [30]. The EBSD measurements were performed at a working distance of 15 mm with an acceleration voltage of 20 kV, 2 nA current and 6x6 binning. First an overview scan was carried out to identify areas of interest and then a detailed scan with a size of $9 \times 9 \mu\text{m}^2$ and a smaller step size of 25 nm was conducted. The data evaluation for both EBSD and TKD was carried out with the TSL OIM Analysis 7 software without using any data clean-ups. The chemical composition of the M-A constituent was determined by APT investigations after extraction of the area of interest in the FIB by means of the standard lift-out method [31]. The last step of the annular milling was performed at 5 kV to minimize gallium implantation. APT was carried out using a local electrode atom probe (Cameca, LEAP 3000X HR) in the voltage mode with a pulse repetition rate of 200 kHz, a pulse fraction of 0.2 and a specimen temperature of 60 K. Imago Visualization and Analysis Software (IVAS) version 3.6 was used for all analyses.

3. Results and Discussion

The holding time for isothermal bainitic transformation at 400°C in the dilatometer was selected sufficiently long (1000 s) in order to complete the bainitic transformation. Thus, no reaction during the second quenching step from this temperature to room temperature was observed, indicating a fully bainitic microstructure. This was also proven by LOM and SEM images, as shown in Fig. 1. The microstructure after etching with LePera is shown in Fig. 1a, where the dark areas correspond to carbide-free bainite and the white and light brown areas reveal the retained austenite and the M-A constituent, which cannot be distinguished using this etchant. In Fig. 1b a SEM image of the same microstructure after Nital etching is presented with the single constituents marked with arrows. Retained austenite and M-A areas are less severely attacked by the Nital etchant due to their higher carbon content, and therefore their higher chemical potential [32]. Larger angular-shaped islands at the grain boundaries mainly correspond to M-A constituent, whereas smaller circular-shaped islands in the center of the grains are usually austenitic. However, to be completely sure EBSD analysis is necessary.

As already shown in a previous publication of the authors [24] the M-A constituent can be identified in a TEM specimen by a preceded TKD scan as illustrated in Fig. 2. In image quality maps, M-A areas show a darker contrast since the diffraction patterns inside these strained and highly-dislocated areas exhibit a lower quality. Figure 2a shows an image quality map of an area containing a small M-A area, which is mainly martensitic with small amounts of austenite on top, as is apparent from the superimposed phase map shown in Fig. 2b. TKD analysis revealed that the austenite (face-centered cubic, fcc) shares the following orientation relationship with the surrounding bainitic ferrite (body-centered cubic, bcc) as well as with the martensite of the M-A area:



This is indicated by yellow lines in Fig. 2b with a tolerance angle of 4°. The orientation relationship corresponds to the classic Kurdjumov-Sachs or Nishiyama-Wasserman relationship, which differ only by a relative rotation of 5.26° about [011] bcc [33].

Subsequently, exactly the same area was investigated in the TEM as confirmed by the bright field image in Fig. 2c where the same lath boundary is highlighted as in Figs. 2a and 2b.

After this unambiguous identification of the M-A constituent, a detailed TEM diffraction study was carried out. Figure 3a shows the same area as in Fig. 2 at a relative tilt angle of about 8°, where the lath boundary was again used for the alignment. The first selected area electron diffraction (SAED) pattern was recorded in the bainitic ferrite matrix, as indicated in Fig. 3a by SAED 1. As can be seen in Figs. 3b and c, a diffraction pattern corresponding to a bcc crystal structure with a zone axis along $\langle 111 \rangle$ is observed.

3.1. Martensitic part of the M-A constituent

In a next step, SAED patterns inside the M-A area were collected. The electron diffraction pattern of an area which is martensitic according to TKD is illustrated in Fig. 3d. In TEM additionally to the reflections for ferrite/ martensite, reflections according to cementite were found. The schematic diffraction patterns of both phases in Figs. 3e and f are consistent with the following orientation relationship:

$$(12\bar{1}) \text{ bcc} \parallel (3\bar{3}0) \text{ Fe}_3\text{C}$$

$$[113] \text{ bcc} \parallel [331] \text{ Fe}_3\text{C}.$$

The collected experimental data was used to build the stereographic projection in Fig. 4 which indicates that $(5\bar{2}1)$ bcc and (001) Fe_3C as well as (131) bcc and (100) Fe_3C are parallel to each other. This corresponds to one of the variants of the Petch orientation relationship observed between cementite and ferrite [34]. The common orientation relationship indicates that cementite precipitated within the martensitic needle.

As marked in Fig. 3g, another electron diffraction pattern was recorded of a second martensitic lath which is also part of this M-A area. It can be seen in Fig. 3h that, additionally to the main reflections of the $\langle 100 \rangle$ oriented crystal, which are depicted schematically in Fig. 3i, satellites occur. A second grain contributes to the formation of this diffraction pattern as indicated by arrows in Fig. 3h. In general the presence of

planar defects such as stacking faults, line defects such as dislocations, spinodal decomposition or regular arrays of crystal defects can cause satellite spots in electron diffraction patterns as described in [35]. Various authors [36–42] observed satellites in Fe-X-C alloys in martensite prior to tempering. Two distinct stages of aging which precede the conventional stages of tempering could be distinguished. Immediately after the martensitic transformation carbon redistribution into interstitial carbon clusters starts, which is accompanied by the appearance of diffuse spikes around the fundamental diffraction spots [36]. An analysis of the intensity distribution and dark field images affirmed the presence of clusters with a size of 1 nm in high-carbon steels. Prolonged aging above room temperature (about 60-80°C) induces a stress-induced alignment of the carbon clusters, generating a characteristic ‘tweed-like’ or modulated structure which consists of alternating carbon-rich and carbon-poor layers on {102} planes, spaced periodically with intervals of 1-2 nm [36]. The modulated structure is coupled with the observation of satellites at the end of the spikes around the fundamental reflections in the electron diffraction pattern. Ren et al. [42] ascribed the diffuse spikes to varying wavelengths and the satellites to one dominating wavelength of the spinodal decomposition. According to Kusunoki and Nagakura [38], the satellites arise from the periodical displacement of the iron atoms of their original position by the carbon clusters, since the iron atoms contribute the most to diffraction. However, Sandvik and Wayman [43] also observed layered carbon clusters in weak-beam images of high-carbon steels, although only diffuse scattering and no clearly developed satellite reflections occurred in the diffraction pattern. Thus, they suggested that the satellites are a result of stress relaxation within the modulated structure rather than of the modulation itself.

In low-carbon alloys with a M_s temperature well above room temperature, these pre-precipitation processes already start during the cooling process as a result of the very high diffusivity of carbon atoms [41,44]. These auto-tempering effects of the freshly formed martensite can range from carbon segregation to defects, e.g. dislocations, over cluster formation to even carbide precipitation, leading to a reduction in the system’s overall free energy [45–51].

The investigated alloy has a M_s temperature of about 350°C [19]. However, the M-A constituent is enriched in carbon during the isothermal bainitic transformation, and thus they it has a lower M_s temperature. Therefore, the chemical composition of the M-A constituent was determined by APT. For a site-specific preparation, the M-A areas were again identified based on their lower image quality in a conventional EBSD scan of a bulk specimen and subsequently extracted by a FIB lift-out, as indicated in Fig. 5. The chemical composition in Table 2 reveals that the carbon concentration is elevated to 0.54 mass% (2.42 at%) and also the manganese and silicon concentration are slightly enhanced. Based on the equation [52]

$$M_s = 539 - 423 * C - 30.4 * Mn - 7.5 * Si + 30 * Al \text{ (in mass\%)}$$

the M_s temperature for the M-A constituent was determined to be approximately 214°C. This still rather high transformation temperature entails auto-tempering of the fresh martensite immediately after its formation during cooling to room temperature. Thus, it is assumed, that the two martensitic laths observed by TEM represent different auto-tempering (followed by aging) stages. The martensitic lath which transformed earlier already exhibits small cementite precipitates due to the longer time at higher temperatures, whereas the lath transformed later only reveals carbon clusters, as inferred from the satellites present in Fig. 3h.

Early APT studies [39,53] tried to visualize the periodic carbon clusters. Taylor et al. [39] could show that after prolonged room temperature aging of Fe-Ni-C steels alternating carbon-rich (~11 at%) and carbon-poor (~0.2 at%) bands are detected which correspond to the modulated structure observed in TEM. Although previous electron diffraction studies [54] suggested a tetragonal Fe_4C superstructure of the carbon-rich phase, the carbon concentration obtained by APT rather corresponds to Fe_8C and, therefore, an imperfect form of the α'' - $Fe_{16}N_2$ structure was proposed [39]. The continuous increase in compositional amplitude as well as the increase of wavelength of the modulation over time are characteristic for a spinodal mechanism. It is assumed that this structural modulation by spinodal decomposition is a general feature of Fe-X-C martensite during aging [39]. These findings agree well with the observations by TEM as spinodal decomposition brings about satellite spots in electron diffraction patterns, since it

represents a periodic displacement of the regular crystal lattice [35]. More recently, Zhu et al. [55] observed a fine striated structure of carbon-rich regions by APT in a Fe-Ni-C and a high-carbon steel after room temperature aging, also supporting the theory of a structural modulation. On the other hand, Kim et al. [56] found no evidence of Fe_{16}C_2 formed by spinodal decomposition in Fe-Ni-C steels by high-resolution X-ray diffraction using synchrotron radiation and related the carbon-enriched areas observed by APT to segregation to defects, since their appearance is linear and the distance between the enriched areas correlates well to the spacing between dislocations. However, the product of spinodal decomposition and segregation to defects are difficult to distinguish using APT since both lead to a similar local carbon enrichment.

In our case, the challenge to investigate the carbon distribution inside the martensite is even higher. First of all, the studied material is an industrial, low-alloyed steel, possessing a high M_s temperature. Thus, auto-tempering and aging effects inevitably occur during cooling, specimen preparation and storage. Secondly, the M-A areas only represent a small fraction in carbide-free bainitic steels. After site-specific APT specimen preparation in the FIB the carbon distribution can be investigated. However, no information upon the tempering and aging stage is available.

The M-A area for the lift-out in Fig. 5 comprises some austenite and various martensitic laths as can be seen in the EBSD phase map and the inverse pole figures of ferrite and austenite. Results of an APT specimen of that area are depicted in Fig. 6. From visual inspection of the carbon atom maps in Fig. 6a a heterogeneous distribution and a distinct enrichment of carbon at an interface can be ascertained. Since carbon is known to segregate to phase and grain boundaries, it is assumed that the tip contains two martensitic laths. Chemical analysis of the upper and lower martensitic lath yields a carbon concentration of 2.75 at% and 1.88 at%, respectively. Frequency distribution analyses using a bin size of 200 of the carbon atoms are plotted in Figs. 6b and d, where the observed distribution is compared to a binomial one in order to detect deviations from homogeneous element distribution. With a statistical confidence of 0.95 the atoms are non-randomly distributed. For better comparison, the Pearson coefficient μ was calculated for both laths, which can be used to follow changes in the degree of segregation between various data sets since it excludes influences from different sample

sizes. A value of μ close to 0 indicates homogenous distribution, whereas 1 indicates a complete association of the solute atoms [57]. For the upper lath a μ -value of 0.35 and for the lower lath a value of 0.47 were obtained for carbon atoms. This indicates a high degree of carbon segregation in both laths. The more pronounced segregation of the lower lath and also its lower carbon concentration can be explained by a higher formation temperature of the martensite during the final quenching step, resulting in more time for auto-tempering effects such as carbon redistribution to defects and formation of carbon clusters. This is consistent with findings by Lerchbacher et al. [58] who also related the degree of carbon segregation in quenched martensite to the formation temperature of the laths, with higher temperatures leading to enhanced segregation. Carbon clusters have also been observed in quenched martensite of transformation-induced plasticity steels [59–61] and bainitic ferrite [62] by APT and are considered as nucleation sites for carbides. The 1D concentration profile in Fig. 6c reveals a carbon enrichment up to 6 at% and a uniform distribution of silicon and manganese across the interface. According to calculations of the M_s temperature [63] a carbon enrichment higher than 4 at% is required to chemically stabilize the austenite against martensite transformation in this alloy. Therefore, the interlath film containing about 6 at% carbon presumably represents retained austenite, as also observed in other studies on martensite [58,64].

3.2. Austenitic part of the M-A constituent

A small part on top of the M-A area remained austenitic after quenching, as can be seen in Fig. 2b. This area was also investigated by TEM (Figs. 7 and 8). The first diffraction pattern of the austenite, with the area indicated by SAED 4 in Fig. 7a, is shown in Fig. 7b. The schematic diffraction pattern of the austenite with a zone axis along $\langle 111 \rangle$ is given in Fig. 7c. Surprisingly, the main reflections are again surrounded by satellites. In order to verify their authenticity, another SAED was recorded in a further zone axis, depicted in Figs. 8a-c. Although the satellites are not as well aligned as in Fig. 7, their presence is undoubtedly. Figure 8d illustrates a dark field image using a main reflection as indicated in Fig. 8b, revealing that the whole austenitic grain is in diffraction condition.

By contrast, when a satellite spot is used for a dark field image, only isolated areas inside the austenitic grain appear bright (Fig. 8e). This is well portrayed in Fig. 8f, where the two dark field images are superimposed. Purely austenitic islands without any martensitic fraction reveal clear diffraction patterns in the absence of any satellite reflections in this steel [63]. Various reasons for the observation of satellites in the austenitic part of the M-A constituent could be possible: (1) the carbon distribution is also heterogeneous as in the martensitic part, (2) there are regular arrays of dislocations induced by the strains due to the martensitic transformation in the adjacent areas or (3) the austenite contains planar defects such as stacking faults. However, the actual cause of the satellites is not yet fully understood and needs further consideration.

In Fig. 9 the findings of the microstructural analysis of the M-A area by TKD and TEM are compared. Generally, the resolution of TKD is determined by the atomic number of the investigated material, the accelerating voltage, the specimen thickness and the specimen tilt [27]. With optimized parameters a resolution significantly below 10 nm can be achieved [25]. Since TKD was used to quickly scan a larger area of the TEM specimen to identify regions of interest for a detailed TEM study, a rather big step size of 60 nm was chosen in order to minimize specimen contamination. Therefore, the aim was not to obtain maximum resolution but to support the subsequent investigations. Nevertheless, both methods indicate an austenitic and martensitic part. The TEM investigation further revealed that the martensitic area consists of two different regions, which seem to be two martensitic laths transformed at different times during quenching. The austenitic part also appears to be affected by the martensitic transformation in close proximity, resulting in some kind of structural modulation.

4. Summary

In this study, a microstructural characterization of the M-A constituent in a carbide-free bainitic steel was carried out by applying various high-resolution techniques. Based on the approach suggested in a previous work of the authors [24], the M-A constituent was successfully identified on TEM specimens by a preceded TKD scan. The subsequent electron diffraction study and dark field imaging of the individual phases combined with

the results from APT provided valuable information regarding the formation history of the M-A areas. Following scientific insights could be gained:

- Both methods, TKD as well as TEM, confirmed the presence of lath martensite and retained austenite in the M-A constituent.
- The martensitic laths show strong auto-tempering and aging effects ranging from carbon clustering, evidenced by satellite reflections in the diffractions patterns, to even cementite precipitation, affirmed by the common orientation relationship of cementite and the parent martensite.
- The austenite belonging to the M-A area also exhibits satellite reflections, whereby their origin needs further consideration.
- APT revealed a heterogeneous carbon distribution inside the M-A areas, with the extent of the segregation depending on the formation temperature of the martensite.

Acknowledgment

Funding of the Austrian BMVIT in the framework of the program “Production of the future” and the “BMVIT Professorship for Industry” is gratefully acknowledged. The authors are thankful to Professor Christina Scheu, Professor Gerhard Dehm and Professor Francisca G. Caballero for fruitful discussion.

Data availability statement

The raw/processed data required to reproduce these findings cannot be shared at this time as the data also forms part of an ongoing study.

Literature

- [1] H.K.D.H. Bhadeshia, D.V. Edmonds, Bainite in silicon steels: New composition property approach - Part 1, *Metal Science*. 17 (1983) 411–419.
- [2] H.K.D.H. Bhadeshia, D.V. Edmonds, Bainite in silicon steels: New composition

property approach - Part 2, *Metal Science*. 17 (1983) 420–425.

- [3] A. Grajcar, R. Kuziak, W. Zalecki, Third generation of AHSS with increased fraction of retained austenite for the automotive industry, *Archives of Civil and Mechanical Engineering*. 12 (2012) 334–341.
- [4] J.G. Speer, F.C.R. Assunção, D.K. Matlock, D. V. Edmonds, The “quenching and partitioning” process: Background and recent progress, *Materials Research*. 8 (2005) 417–423. doi:10.1590/S1516-14392005000400010.
- [5] F.G. Caballero, S. Allain, J. Cornide, J.D. Puerta Velásquez, C. Garcia-Mateo, M.K. Miller, Design of cold rolled and continuous annealed carbide-free bainitic steels for automotive application, *Materials and Design*. 49 (2013) 667–680. doi:10.1016/j.matdes.2013.02.046.
- [6] E. Kozeschnik, H.K.D.H. Bhadeshia, Influence of silicon on cementite precipitation in steels, *Materials Science and Technology*. 24 (2008) 343–347.
- [7] F.G. Caballero, H. Bhadeshia, K.J.A. Mawella, D.G. Jones, P. Brown, Design of novel high strength bainitic steels: Part 2, *Materials Science and Technology*. 17 (2001) 517–522.
- [8] B.P.J. Sandvik, The bainite reaction in Fe-Si-C alloys: The primary stage, *Metallurgical Transactions A*. 13A (1982) 777–787.
- [9] B.P.J. Sandvik, The bainite reaction in Fe-Si-C alloys: The secondary stage, *Metallurgical Transactions A*. 13A (1982) 789–800.
- [10] H.K.D.H. Bhadeshia, D.V. Edmonds, The bainite transformation in a silicon steel, *Metallurgical Transactions A*. 10A (1979) 895–907.
- [11] F.G. Caballero, M.K. Miller, A.J. Clarke, C. Garcia-Mateo, Examination of carbon partitioning into austenite during tempering of bainite, *Scripta Materialia*. 63 (2010) 442–445. doi:10.1016/j.scriptamat.2010.04.049.
- [12] A. Lambert, J. Drillet, A.F. Gourgues, T. Sturel, A. Pineau, Microstructure of martensite austenite constituents in heat affected zones of high strength low alloy steel welds in relation to toughness properties, *Science and Technology of Welding and Joining*. 5 (2000) 168–173.
- [13] E. Mazancova, K. Mazanec, Physical metallurgy characteristics of the M/A constituent formation in granular bainite, *Journal of Materials Processing Technology*. 64 (1997) 287–292.
- [14] N. Huda, A.R.H. Midawi, J. Gianetto, R. Lazor, A.P. Gerlich, Influence of martensite-austenite (MA) on impact toughness of X80 line pipe steels, *Materials Science and Engineering A*. 662 (2016) 481–491. doi:10.1016/j.msea.2016.03.095.
- [15] H.F. Lan, L.X. Du, R.D.K. Misra, Effect of microstructural constituents on strength-toughness combination in a low carbon bainitic steel, *Materials Science and Engineering A*. 611 (2014) 194–200. doi:10.1016/j.msea.2014.05.084.
- [16] V. Biss, R.L. Cryderman, Martensite and retained austenite in hot-rolled, low-carbon bainitic steels, *Metallurgical and Materials Transactions B*. 2 (1971) 2267–2276. doi:10.1007/BF02917559.

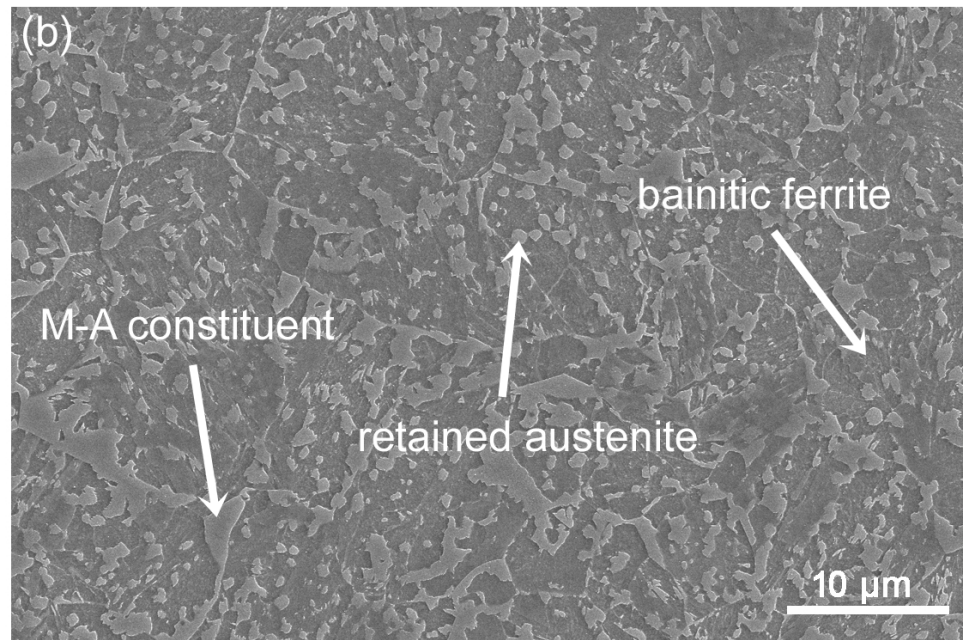
- [17] P. Mohseni, J.K. Solberg, M. J.Karlsen, O.M. Akselsen, E. Ostby, Cleavage fracture initiation at M-A constituents in intercritically coarse-grained heat-affected zone of a HSLA steel, *Metallurgical and Materials Transactions A*. 45A (2014) 384–394.
- [18] C.W. Li, L.Z. Han, X.M. Luo, Q.D. Liu, J.F. Gu, Fine structure characterization of martensite/austenite constituent in low-carbon low-alloy steel by transmission electron forward scatter diffraction, *Journal of Microscopy*. 264 (2016) 252–258. doi:10.1111/jmi.12465.
- [19] C. Hofer, H. Leitner, F. Winkelhofer, H. Clemens, S. Primig, Structural characterization of “carbide-free” bainite in a Fe–0.2C–1.5Si–2.5Mn steel, *Materials Characterization*. 102 (2015) 85–91. doi:10.1016/j.matchar.2015.02.020.
- [20] M.J. Santofimia, R.H. Petrov, L. Zhao, J. Sietsma, Microstructural analysis of martensite constituents in quenching and partitioning steels, *Materials Characterization*. 92 (2014) 91–95. doi:http://dx.doi.org/10.1016/j.matchar.2014.03.003.
- [21] M.K. Miller, K.F. Russell, Atom probe specimen preparation with a dual beam SEM/FIB miller, *Ultramicroscopy*. 107 (2007) 761–766. doi:10.1016/j.ultramic.2007.02.023.
- [22] K.E. Knipling, D.J. Rowenhorst, R.W. Fonda, G. Spanos, Effects of focused ion beam milling on austenite stability in ferrous alloys, *Materials Characterization*. 61 (2010) 1–6. doi:10.1016/j.matchar.2009.09.013.
- [23] A. Basa, C. Thaulow, A. Barnoush, Chemically induced phase transformation in austenite by focused ion beam, *Metallurgical and Materials Transactions A*. 45 (2014) 1189–1198. doi:10.1007/s11661-013-2101-4.
- [24] C. Hofer, V. Bliznuk, A. Verdiere, R. Petrov, F. Winkelhofer, H. Clemens, S. Primig, Correlative microscopy of a carbide-free bainitic steel, *Micron*. 81 (2016) 1–7. doi:10.1016/j.micron.2015.10.008.
- [25] P.W. Trimby, Orientation mapping of nanostructured materials using transmission Kikuchi diffraction in the scanning electron microscope, *Ultramicroscopy*. 120 (2012) 16–24. doi:http://dx.doi.org/10.1016/j.ultramic.2012.06.004.
- [26] R.R. Keller, R.H. Geiss, Transmission EBSD from 10 nm domains in a scanning electron microscope, *Journal of Microscopy*. 245 (2012) 245–251. doi:10.1111/j.1365-2818.2011.03566.x.
- [27] G.C. Sneddon, P.W. Trimby, J.M. Cairney, Transmission Kikuchi diffraction in a scanning electron microscope: A review, *Materials Science and Engineering R*. 110 (2016) 1–12. doi:10.1016/j.mser.2016.10.001.
- [28] F.S. LePera, Improved etching technique to emphasize martensite and bainite in high-strength dual-phase steel, *Journal of Metals*. (1980) 38–39.
- [29] T.A. Dzigrashvili, Computer simulation of electron diffraction patterns and stereographic projections, *Microscopy and Analysis*. 22 (2008) 5–7.
- [30] C. Hofer, H. Clemens, S. Primig, Preparation of carbide-free bainitic steels for EBSD investigations, *Practical Metallography*. 52 (2015) 384–395.
- [31] M.K. Miller, K.F. Russell, G.B. Thompson, Strategies for fabricating atom probe

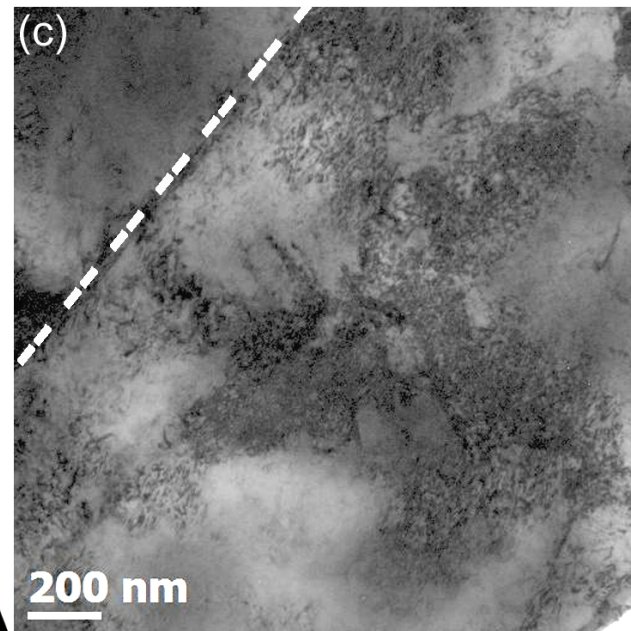
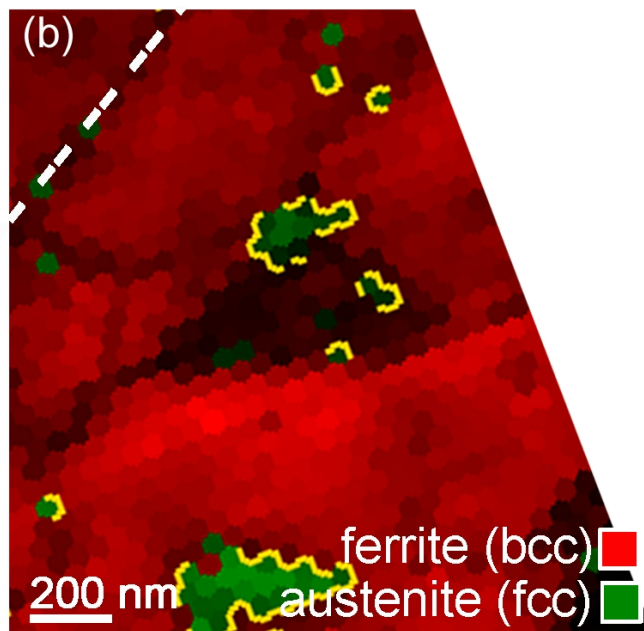
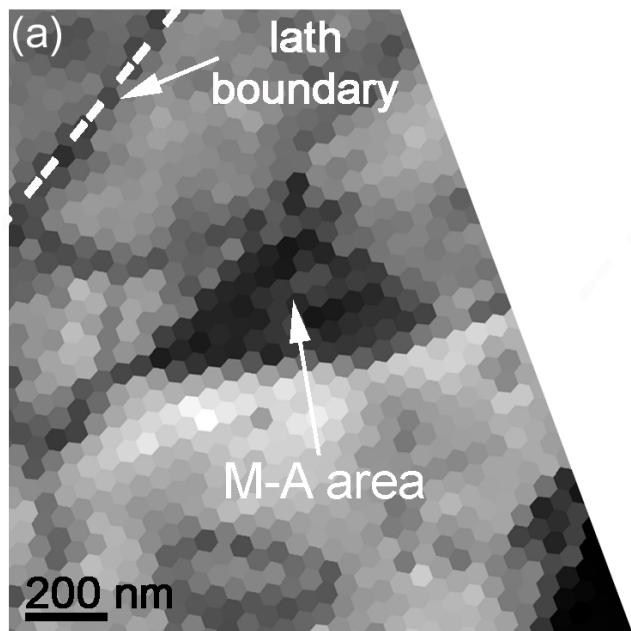
- specimens with a dual beam FIB, *Ultramicroscopy*. 102 (2005) 287–298. doi:10.1016/j.ultramicro.2004.10.011.
- [32] J. Angeli, E. Füreder, M. Panholzer, A.C. Kneissl, Etching techniques for characterizing the phases of low-alloy dual-phase and TRIP steels, *Practical Metallography*. 43 (2006) 489–504.
- [33] H.K.D.H. Bhadeshia, *Bainite in steels*, 2nd ed., The Institute of Materials, London, 2001.
- [34] N.J. Petch, The orientation relationships between cementite and alpha-iron, *Acta Crystallographica*. 6 (1953) 96.
- [35] J.W. Edington, *Electron diffraction in the electron microscope*, Phillips, Arlington, VA, 1975.
- [36] S. Nagakura, Y. Hirotsu, M. Kusunoki, T. Suzuki, Y. Nakamura, Crystallographic study of the tempering of martensitic carbon steel by electron microscopy and diffraction, *Metallurgical Transactions A*. 14 (1983) 1025–1031. doi:10.1007/BF02670441.
- [37] S. Nagakura, M. Toyoshima, Crystal structure and morphology of the ordered phase in iron-carbon martensite, *Transactions of the Japan Institute of Metals*. 20 (1979) 100–109.
- [38] M. Kusunoki, S. Nagakura, Modulated structure of iron-carbon martensite studied by electron microscopy and diffraction, *Journal of Applied Crystallography*. 14 (1981) 329–336. doi:10.1107/S0021889881009485.
- [39] K.A. Taylor, L. Chang, G.B. Olson, G.D.W. Smith, M. Cohen, J.B. Vander Sande, Spinodal decomposition during aging of Fe-Ni-C martensites, *Metallurgical Transactions A*. 20 (1989) 2717–2737. doi:10.1007/BF02670166.
- [40] K. Han, M.J. van Genderen, A. Böttger, H.W. Zandbergen, E.J. Mittemeijer, Initial stages of Fe-C martensite decomposition, *Philosophical Magazine A*. 81 (2001) 741–757. doi:10.1080/01418610108212169.
- [41] M.J. van Genderen, M. Isac, A. Böttger, E.J. Mittemeijer, Aging and tempering behavior of iron-nickel-carbon and iron-carbon martensite, *Metallurgical and Materials Transactions A*. 28 (1997) 545–561. doi:10.1007/s11661-997-0042-5.
- [42] S.B. Ren, T. Tadaki, K. Shimizu, X.T. Wang, Electron diffraction study of aging processes in Fe-1.83 wt pct C martensite at room temperature, *Metallurgical and Materials Transactions A*. 26 (1995) 2001–2005. doi:10.1007/BF02670672.
- [43] B.P.J. Sandvik, C.M. Wayman, Direct observations of carbon clusters in a high-carbon martensitic steel, *Metallography*. 16 (1983) 429–447. doi:10.1016/0026-0800(83)90031-9.
- [44] R.C. Thomson, M.K. Miller, An atom probe study of cementite precipitation in autotempered martensite in an Fe-Mn-C alloy, *Applied Surface Science*. 94–95 (1996) 313–319. doi:http://dx.doi.org/10.1016/0169-4332(95)00392-4.
- [45] A.H. Cottrell, B.A. Bilby, Dislocation theory of yielding and strain ageing of iron, *Proceedings of the Physical Society. Section A*. 62 (1949) 49–62. doi:10.1088/0370-1298/62/1/308.

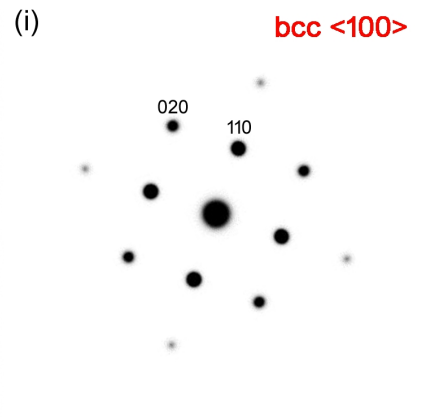
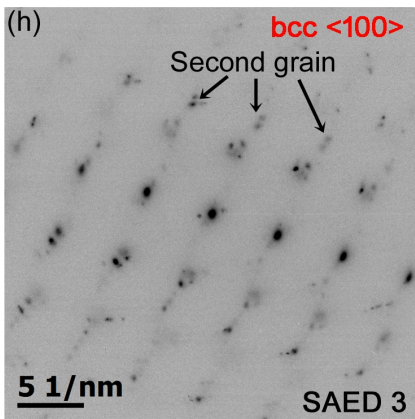
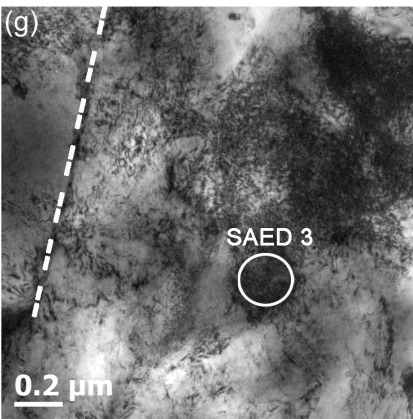
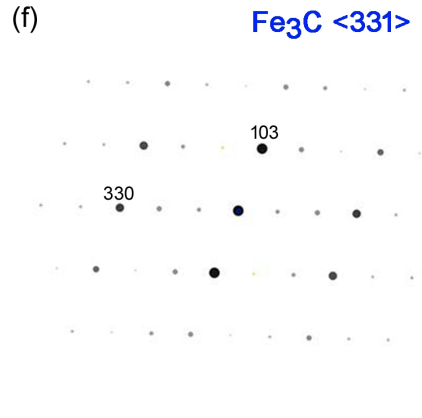
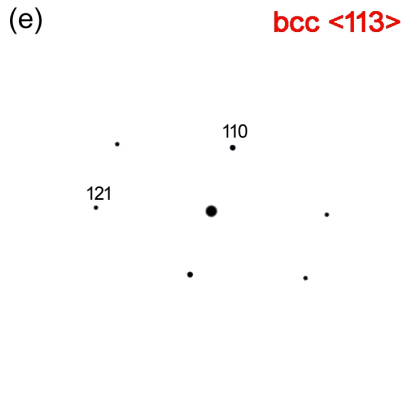
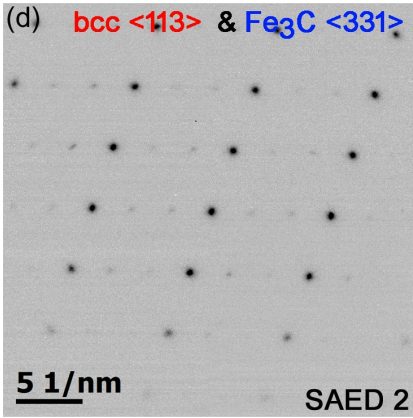
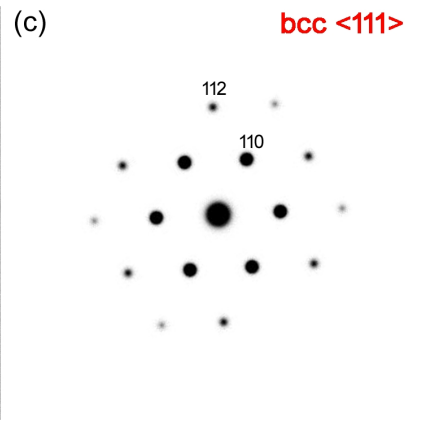
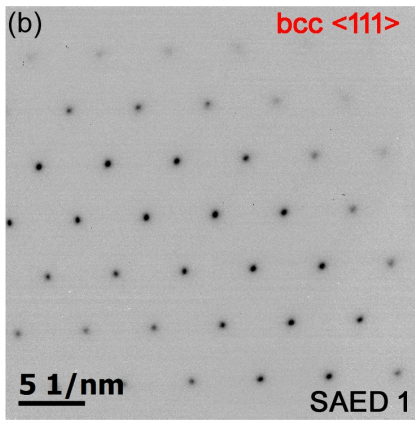
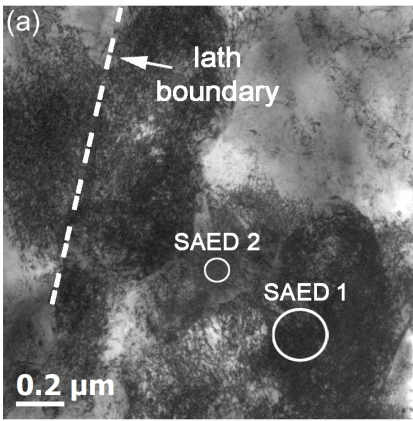
- [46] G.R. Speich, Tempering of low-carbon martensite, *Transactions of the Metallurgical Society of AIME*. 245 (1969) 2553–2564.
- [47] D. Kalish, M. Cohen, Structural changes and strengthening in the strain tempering of martensite, *Materials Science and Engineering*. 6 (1970) 156–166.
- [48] R.W.K. Honeycombe, H.K.D.H. Bhadeshia, *Steels - Microstructure and properties*, 2nd ed., Butterworth-Heinemann, Oxford, 1995.
- [49] B. Hutchinson, J. Hagström, O. Karlsson, D. Lindell, M. Tornberg, F. Lindberg, M. Thuvander, Microstructures and hardness of as-quenched martensites (0.1-0.5%C), *Acta Materialia*. 59 (2011) 5845–5858. doi:10.1016/j.actamat.2011.05.061.
- [50] G.A. Thomas, F. Danoix, J.G. Speer, S.W. Thompson, F. Cuvelly, Carbon atom redistribution during quenching and partitioning, *ISIJ International*. 54 (2014) 2900–2906.
- [51] G. Krauss, Tempering of lath martensite in low and medium carbon steels: Assessment and challenges, *Steel Research International*. 87 (2017) 1–18. doi:10.1002/srin.201700038.
- [52] J. Mahieu, J. Maki, B.C. De Cooman, S. Claessens, Phase transformation and mechanical properties of Si-free CMnAl transformation-induced plasticity-aided steel, *Metallurgical and Materials Transactions A*. 33A (2002) 2573–2580.
- [53] M.K. Miller, P.A. Beaven, S.S. Brenner, G.D.W. Smith, An atom probe study of the aging of iron-nickel-carbon martensite, *Metallurgical Transactions A*. 14 (1983) 1021–1024.
- [54] V.I. Izotov, L.M. Utevskiy, Structure of the martensite crystals of high-carbon steel, *Fizika Metallov i Metallovedenie*. 25 (1968) 98–110.
- [55] C. Zhu, A. Cerezo, G.D.W. Smith, Carbide characterization in low-temperature tempered steels, *Ultramicroscopy*. 109 (2009) 545–552. doi:10.1016/j.ultramic.2008.12.007.
- [56] B. Kim, J. Sietsma, M.J. Santofimia, Thermodynamic aspects of carbon redistribution during ageing and tempering of Fe–Ni–C alloys, *Philosophical Magazine*. 96 (2016) 2632–2648. doi:10.1080/14786435.2016.1211790.
- [57] M.P. Moody, L.T. Stephenson, A. V. Ceguerra, S.P. Ringer, Quantitative binomial distribution analyses of nanoscale like-solute atom clustering and segregation in atom probe tomography data, *Microscopy Research and Technique*. 71 (2008) 542–550. doi:10.1002/jemt.20582.
- [58] C. Lerchbacher, S. Zinner, H. Leitner, Atom probe study of the carbon distribution in a hardened martensitic hot-work tool steel X38CrMoV5-1, *Micron*. 43 (2012) 818–826. doi:10.1016/j.micron.2012.02.005.
- [59] E.V. Pereloma, I.B. Timokhina, K.F. Russell, M.K. Miller, Characterization of clusters and ultrafine precipitates in Nb-containing C-Mn-Si steels, *Scripta Materialia*. 54 (2006) 471–476. doi:10.1016/j.scriptamat.2005.10.008.
- [60] E.V. Pereloma, M.K. Miller, I.B. Timokhina, On the decomposition of martensite during bake hardening of thermomechanically processed transformation-induced plasticity steels, *Metallurgical and Materials Transactions A*. 39 (2008) 3210–3216.

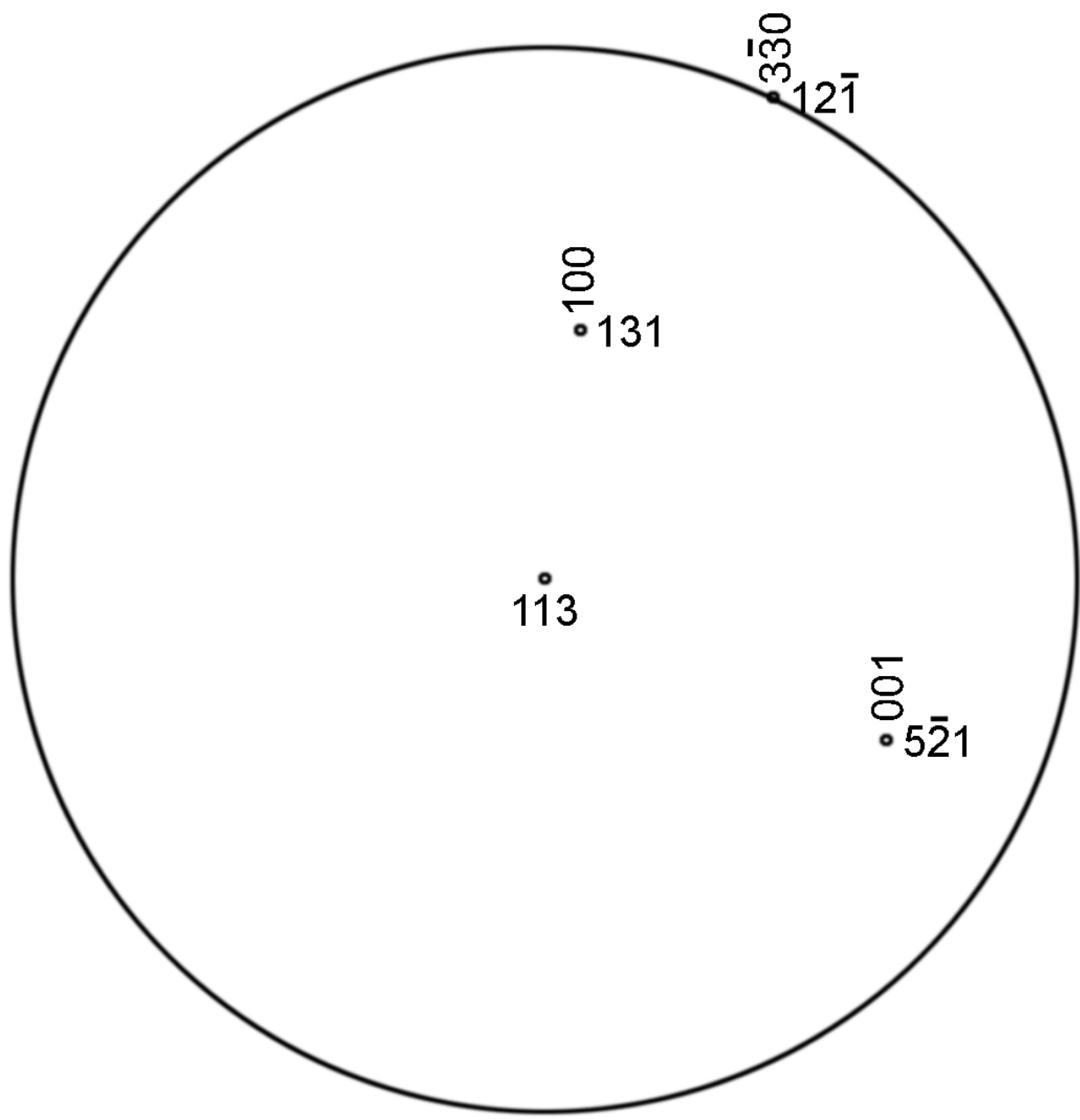
doi:10.1007/s11661-008-9663-6.

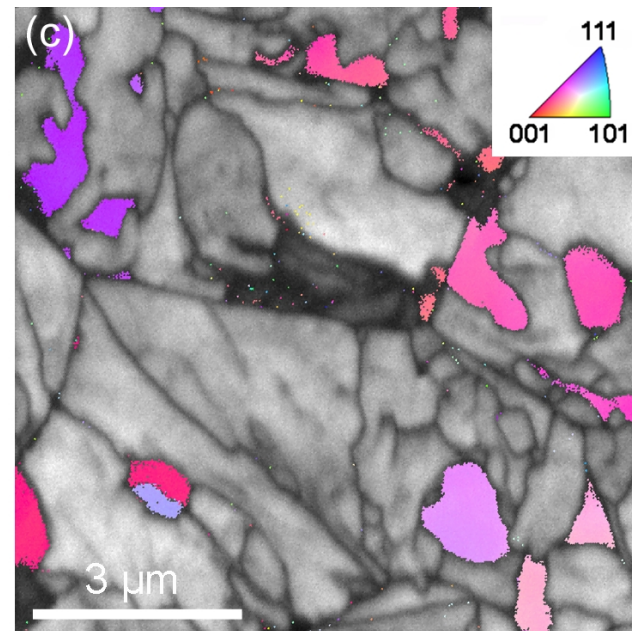
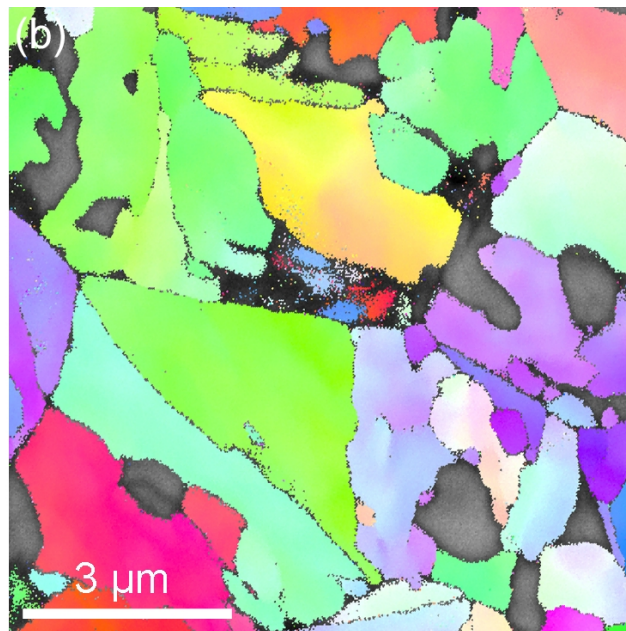
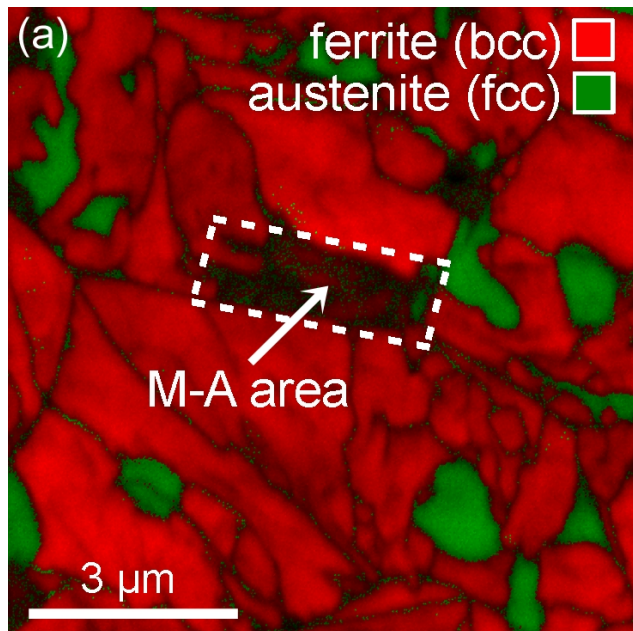
- [61] E.V. Pereloma, S.P. Ringer, I.B. Timokhina, P.D. Hodgson, Observations of decomposition of martensite during heat treatment of steels using atom probe tomography, in: ESOMAT 2009, 2009. doi:10.1051/esomat/20090.
- [62] F.G. Caballero, M.K. Miller, C. Garcia-Mateo, Carbon supersaturation of ferrite in a nanocrystalline bainitic steel, *Acta Materialia*. 58 (2010) 2338–2343. doi:10.1016/j.actamat.2009.12.020.
- [63] C. Hofer, F. Winkelhofer, H. Clemens, S. Primig, Morphology change of retained austenite during austempering of carbide-free bainitic steel, *Materials Science and Engineering A*. 664 (2016) 236–246. doi:10.1016/j.msea.2016.04.005.
- [64] A.M. Sherman, G.T. Eldis, M. Cohen, The aging and tempering of iron-nickel-carbon martensites, *Metallurgical Transactions A*. 14 (1983) 995–1005.

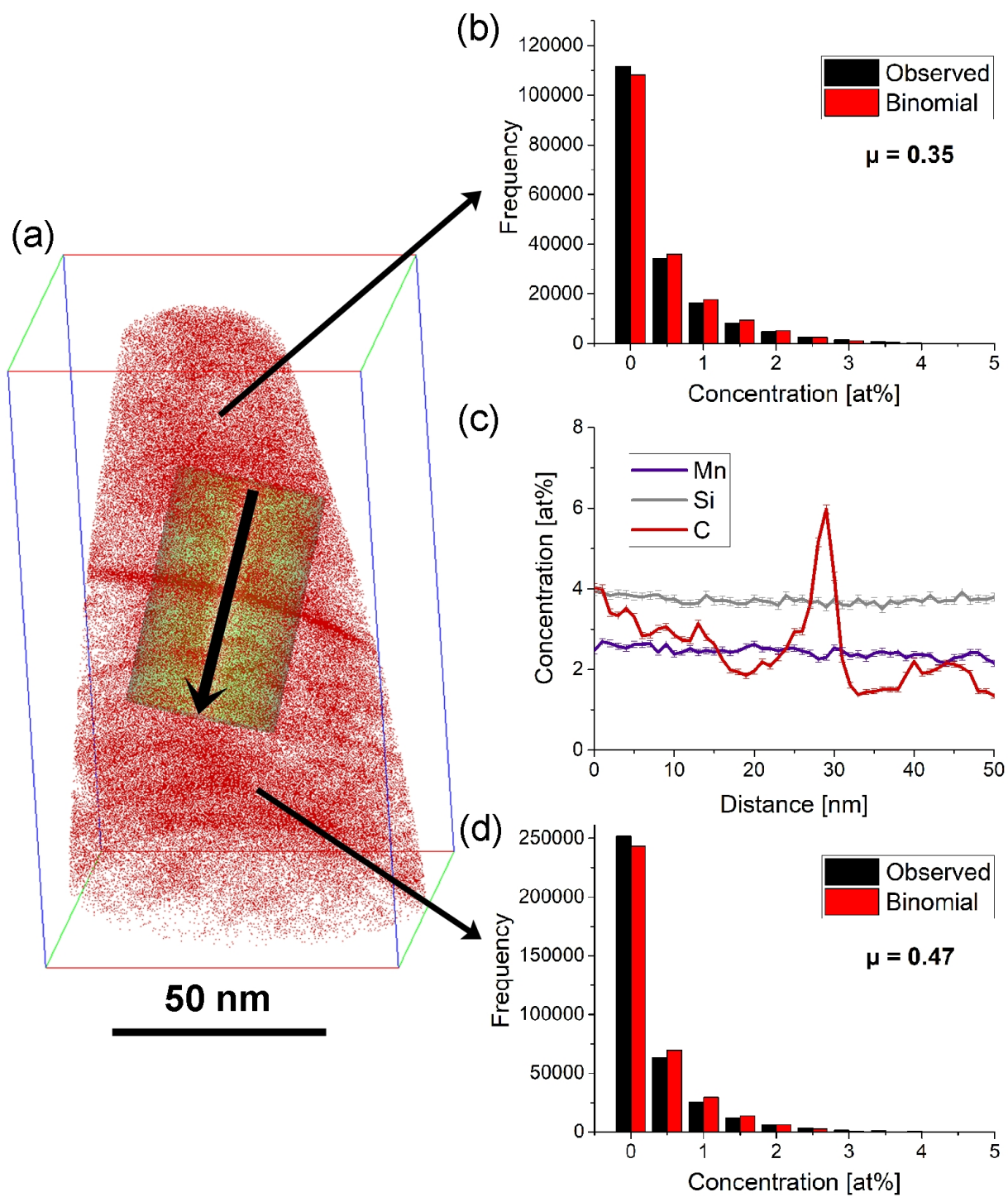


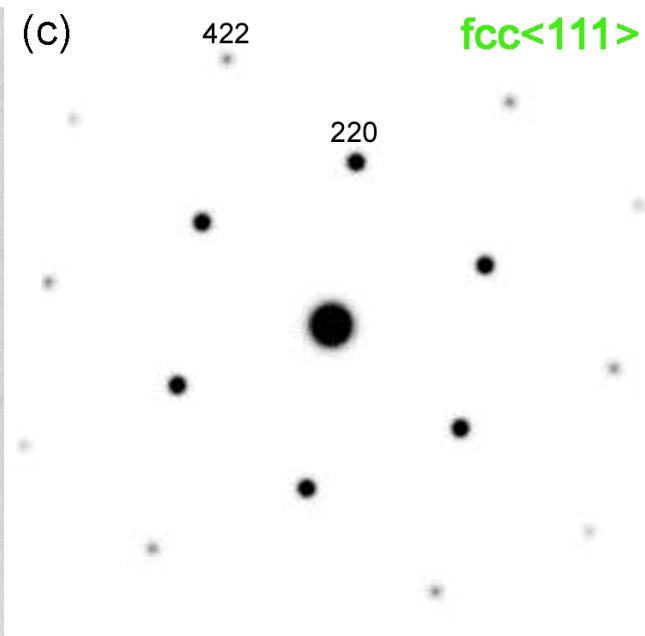
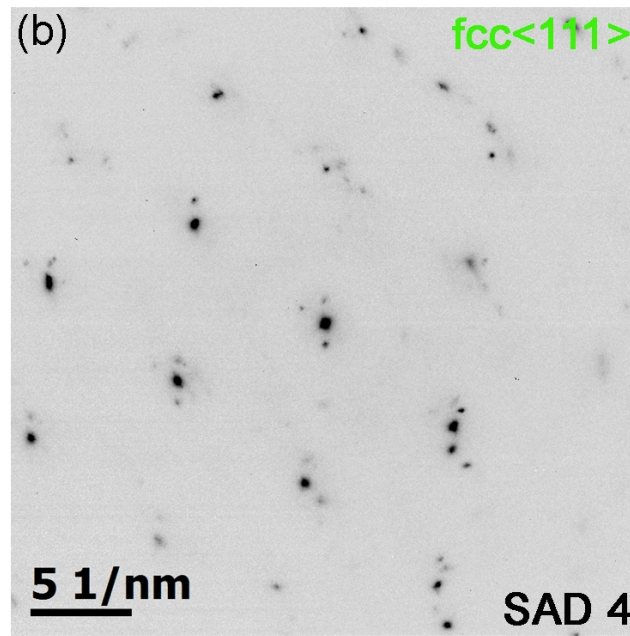
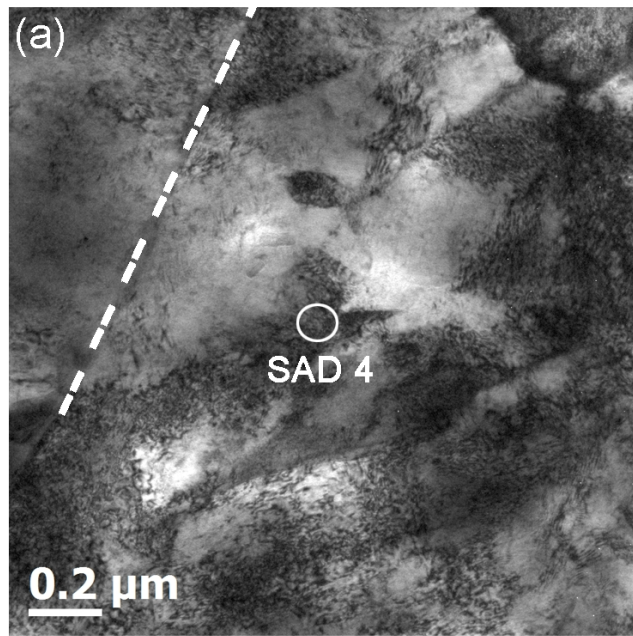


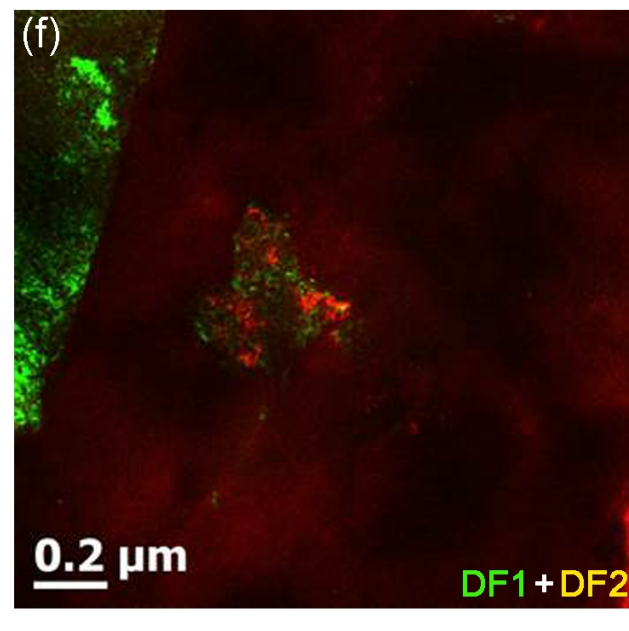
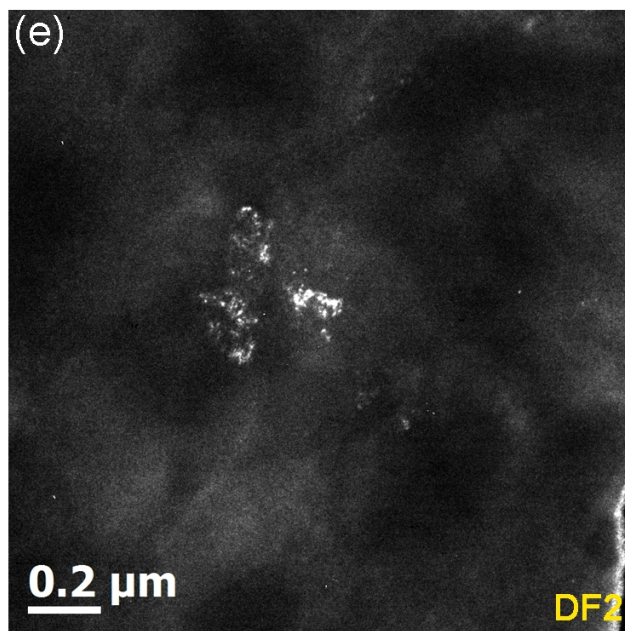
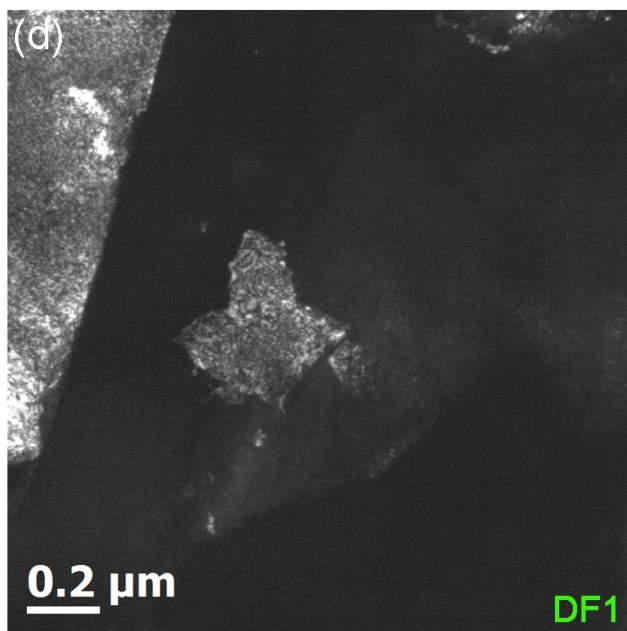
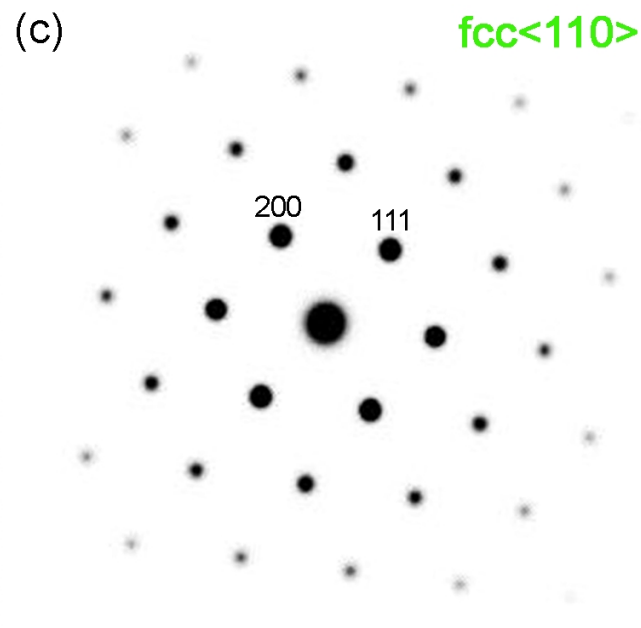
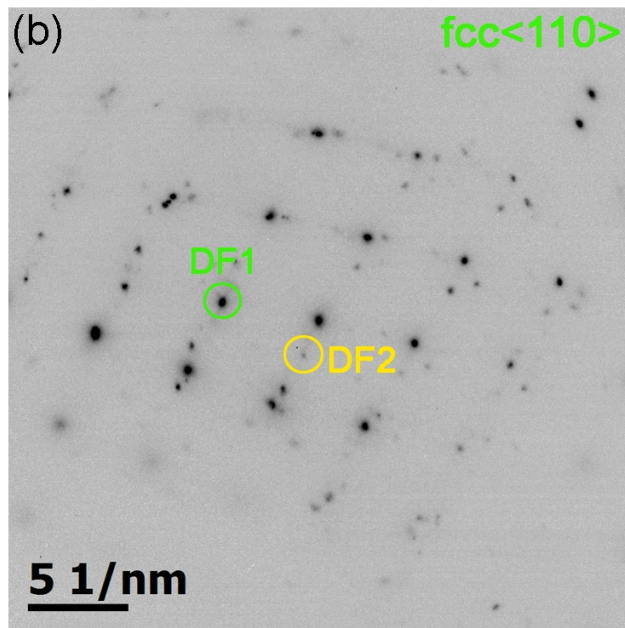
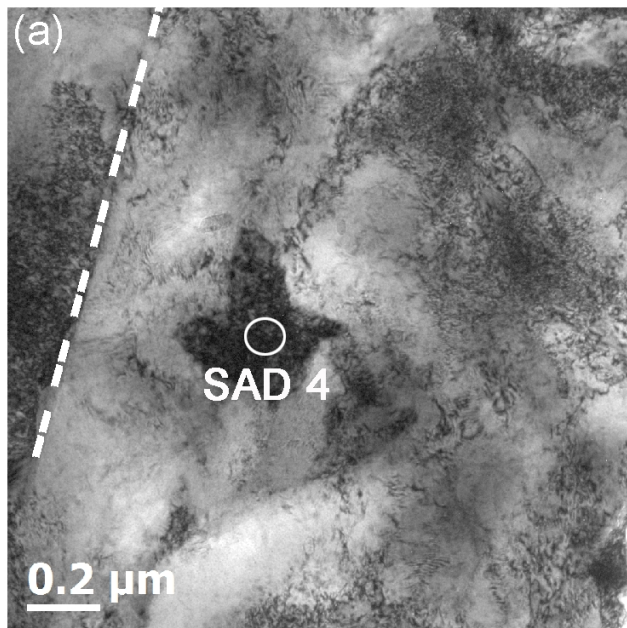












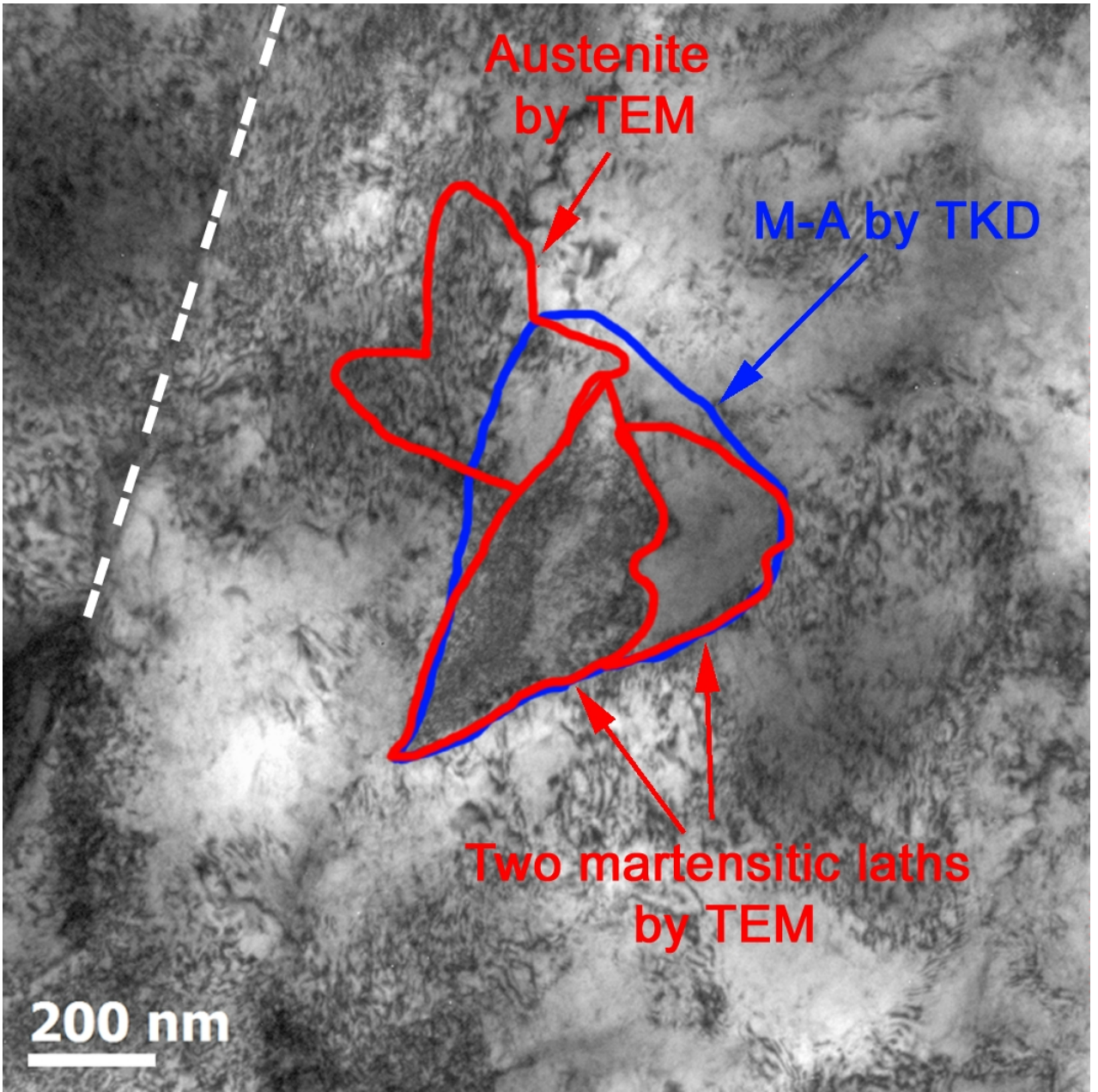


Figure captions

Fig. 1. (a) LOM image after LePera etching and (b) SEM secondary electron image after Nital etching of the sample isothermally transformed at 400°C for 1000 s.

Fig. 2. (a) Image quality map of the preceded TKD scan; (b) Image quality map superimposed with a phase map. The orientation relationship with a tolerance angle of 4° is highlighted by a yellow line. (c) Bright field image of the same area obtained in the TEM. The same lath boundary is indicated by the dashed line in all images. Reprinted in a similar way from [24], Copyright 2016, with permission from Elsevier.

Fig. 3. (a) TEM bright field image of the same area as in Fig. 2 with a different relative tilt of about 8°; (b) SAED 1 of the area indicated in (a); (c) schematic diffraction pattern of the ferrite exhibiting a $\langle 111 \rangle$ zone axis; (d) SAED 2 of the area indicated in (a); (e) schematic diffraction pattern of ferrite with a $\langle 113 \rangle$ zone axis; (f) schematic diffraction pattern of cementite exhibiting a $\langle 331 \rangle$ zone axis; (g) bright field image of the same area with a relative tilt of about 5°; (h) SAED 3 of the area indicated in (g); (i) schematic diffraction pattern of ferrite with a $\langle 100 \rangle$ zone axis. Figs. (g) to (i) are reprinted from [24], Copyright 2016, with permission from Elsevier.

Fig. 4. Stereographic projection of the experimental data, showing that cementite (vertical) and martensite (horizontal) share a common Petch orientation relationship.

Fig. 5. EBSD measurement of a bulk specimen: (a) image quality map superimposed with a phase map (the area of the FIB lift-out is indicated by a dashed square), (b) inverse pole figure of ferrite and (c) inverse pole figure of austenite.

Fig. 6. (a) Carbon atom map of an APT measurement of the area indicated in Fig. 5; (b) frequency distribution analysis of carbon of the upper area; (c) 1-D concentration

profile along the cylinder as indicated in (a). Due to the used scaling Fe is not shown.
(d) Frequency distribution analysis of carbon of the lower area.

Fig. 7. (a) Bright field image of the same area as in Fig. 2c with a relative tilt of about 25°; (b) SAED 4 of the area indicated in (a); (c) schematic diffraction pattern of austenite exhibiting a $\langle 111 \rangle$ zone axis.

Fig. 8. (a) Bright field image of the same area as in Fig. 2c with a relative tilt of about 10°; (b) SAED 5 of the area indicated in (a); (c) schematic diffraction pattern of austenite exhibiting a $\langle 110 \rangle$ zone axis; (d) dark field image using a main spot of the diffraction pattern in (b); (e) dark field image using a satellite spot as indicated in (b); (f) superimposition of the dark field images in (d) and (e).

Fig. 9. Comparison of the microstructural analysis of the M-A area based on TEM and TKD.

Table 1

Chemical composition of the investigated Fe-0.2C-1.5Si-2.5Mn steel in mass% and at%.

	Fe	Mn	Si	C
mass%	Bal.	2.47	1.51	0.22
at%	Bal.	2.45	2.93	1.00

Table 2

Chemical composition of the M-A area depicted in Fig. 5 in mass% and at%.

	Fe	Mn	Si	C
mass%	Bal.	2.71	1.93	0.54
at%	Bal.	2.64	3.69	2.42